Geochemistry, Geophysics, Geosystems

RESEARCH ARTICLE
10.1029/2020GC009052

Accessory Mineral Eu Anomalies in Suprasolidus Rocks: Beyond Feldspar

R. M. Holder[1,2], **C. Yakymchuk**[3], **and D. R. Viete**[2]

[1]Department of Earth and Environmental Sciences, University of Michigan, Ann Arbor, MI, USA, [2]Department of Earth and Planetary Sciences, Johns Hopkins University, Baltimore, MD, USA, [3]Department of Earth and Environmental Sciences, University of Waterloo, Waterloo, Ontario, Canada

Key Points:
- Eu anomalies in suprasolidus rocks record any process that changes the relative availability of Eu^{2+} and Eu^{3+}, not just feldspar growth
- Disequilibrium is required for feldspar growth to strongly influence accessory mineral Eu anomalies
- Comparing accessory mineral Eu anomalies and Sr concentrations leads to more robust interpretation than evaluating Eu anomalies alone

Supporting Information:
- Supporting Information S1
- Data Set S1

Correspondence to:
R. M. Holder,
roholder@umich.edu

Citation:
Holder, R. M., Yakymchuk, C., & Viete, D. R. (2020). Accessory mineral Eu anomalies in suprasolidus rocks: Beyond feldspar. *Geochemistry, Geophysics, Geosystems*, *21*, e2020GC009052. https://doi.org/10.1029/2020GC009052

Received 24 MAR 2020
Accepted 25 JUN 2020
Accepted article online 11 JUL 2020

Author Contributions:
Conceptualization: R. M. Holder
Data curation: R. M. Holder
Formal analysis: R. M. Holder, C. Yakymchuk
Funding acquisition: D. R. Viete
Methodology: R. M. Holder, C. Yakymchuk
Resources: D. R. Viete
Visualization: R. M. Holder, D. R. Viete
Writing - original draft: R. M. Holder
Writing – review & editing: C. Yakymchuk, D. R. Viete

Abstract Accessory mineral Eu anomalies (Eu/Eu*) are routinely measured to infer changes in the amount of feldspar over time, allowing accessory mineral U-Pb dates to be linked to the progressive crystallization of igneous and metamorphic rocks and, by extension, geodynamic processes. However, changes in Eu/Eu* can reflect any process that changes the relative availability of Eu^{2+} and Eu^{3+}. We constructed partitioning budgets for Sm, Eu^{2+}, Eu^{3+}, and Gd in suprasolidus metasedimentary rocks to investigate processes that can influence accessory mineral Eu anomalies. We modeled three scenarios: (1) closed-system, equilibrium crystallization; (2) fractionation of Eu by feldspar growth during melt crystallization; and (3) removal of Eu by melt extraction. In the closed-system equilibrium model, accessory mineral Eu/Eu* changes as a function of fO_2 and monazite stability; Eu/Eu* changes up to 0.3 over a pressure-temperature range of 4–12 kbar and 700–950°C. Fractionation of Eu by feldspar growth is modeled to decrease accessory mineral Eu/Eu* by ~0.05–0.15 per 10 wt% feldspar crystallized. Melt extraction has a smaller effect; removal of 10% melt decreases accessory mineral Eu/Eu* in the residue by ≤0.05. Although these models demonstrate that fractionation of Eu by feldspar growth can be a dominant control on a rocks u budget, they also show that the common interpretation that Eu/Eu* only records feldspar growth and breakdown is an oversimplification that could lead to incorrect interpretation about the duration and rates of tectonic processes. Consideration of other processes that influence Eu anomalies will allow for a broader range of geological processes to be investigated by petrochronology.

Plain Language Summary Metamorphic rocks—rocks in which new minerals grew in response to increase in pressure and temperature related to deep burial or subduction—and igneous rocks—rocks that formed as magmas cool and crystallize—provide a direct record of how Earth's continents have moved and changed through time. To read this record, geologists need to be able to measure the ages of metamorphism and magmatism: When did it happen? How long did it last? How does it relate to other rocks around the world? A common approach to addressing these questions is using U-Pb dating of the minerals zircon, monazite, and apatite. The elements these minerals incorporate are indicative of how hot and how deep in the Earth they were when they grew. In this study we explore how geologists can use the concentrations of the element Europium (Eu) in these minerals to provide new insights into the geological meaning of U-Pb dates, leading to more robust interpretations of Earth's plate tectonic history.

1. Introduction

Trace element concentrations and ratios in accessory minerals can be used to (semi-)quantitatively link accessory mineral growth to the growth and breakdown of major phases (e.g., Bea & Montero, 1999; Buick et al., 2006; Cioffi et al., 2019; Finger & Krenn, 2007; Foster et al., 2000, 2002; Garber et al., 2017; Hacker et al., 2019; Hermann & Rubatto, 2003; Hokada & Harley, 2004; Kelly et al., 2006; Kelly & Harley, 2005; Mottram et al., 2014; Pyle & Spear, 1999; Rubatto, 2002; Rubatto et al., 2006; Rubatto & Hermann, 2007; Taylor et al., 2015; Warren et al., 2019) (Figure 1). This approach—along with trace element thermobarometers (Ferry & Watson, 2007; Gratz & Heinrich, 1997; Hayden et al., 2008; Pyle et al., 2001; Seydoux-Guillaume et al., 2002; Thomas et al., 2015; Tomkins et al., 2007; Wark & Watson, 2006) and modeling of accessory mineral stability (Janots et al., 2007; Kelsey et al., 2008; Kohn et al., 2015; Shrestha et al., 2019; Spear, 2010; Spear & Pyle, 2010; Yakymchuk, 2017; Yakymchuk et al., 2017; Yakymchuk & Brown, 2014)—can be combined with in situ U-Pb geochronology to infer *P-T-t-d* paths of crystalline rocks that underpin interpretations of their geodynamic significance (e.g., Engi, 2017; Kohn, 2017; Rubatto, 2017;

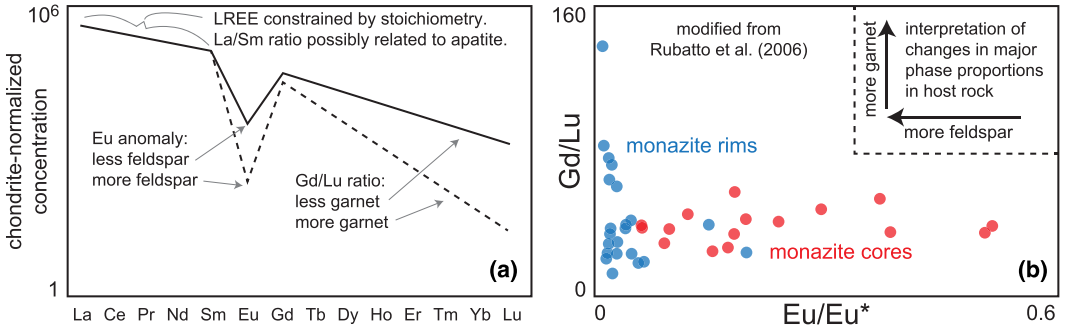

Figure 1. The most applied interpretations of accessory mineral rare-earth-element profiles. (a) Schematic illustration of two monazite REE profiles and how they might be interpreted in the context of progressive crystallization during which the abundance of major minerals changes. (b) Example data set from Rubatto et al. (2006) of monazite core and rim compositions from Mount Stafford, Central Australia. Monazite cores were characterized by low Gd/Lu and high Eu/Eu* compared to monazite rims; this relationship was interpreted to record progressive monazite growth or recrystallization during low-pressure prograde metamorphism as the abundance of alkali feldspar (preferentially incorporates Eu) and then garnet (preferentially incorporates heavy rare earth elements) increased.

Zack & Kooijman, 2017). This multilayered approach to assessing the petrological and geological significance of accessory mineral U-Pb dates forms the foundation of petrochronology (Engi et al., 2017).

In this paper, we address one of the trace element ratios most commonly used in petrochronology: the Eu anomaly ($Eu/Eu^* = Eu_n^{total}/\sqrt{Sm_n \times Gd_n}$, subscript n denotes a normalized concentration; $Eu^{total} = Eu^{3+} + Eu^{2+}$; for this paper, the normalizing values are C. I. chondrite; McDonough & Sun, 1995). Variability in accessory mineral Eu/Eu* ratios are commonly attributed to the growth and breakdown of plagioclase (e.g., Holder et al., 2015) or alkali feldspar (e.g., Mottram et al., 2014; Rubatto et al., 2006, 2013); plagioclase feldspar is particularly sensitive to changes in pressure and useful for investigating high-pressure metamorphism (e.g., O'Brien & Rötzler, 2003), whereas the modes and compositions of both feldspars are sensitive to partial melting. However, mineral Eu/Eu* might be influenced by a range of factors, including the following: (1) bulk-rock Eu/Eu*; (2) the stability of minerals that strongly partition either Eu^{2+} or Eu^{3+}; (3) bulk-rock Eu^{3+}/Eu^{2+}, which depends on fO_2, T, and P; (4) possible differences in the temperature-dependence of partitioning for Eu^{3+} relative to Eu^{2+}; or (5) any process that fractionates Eu^{3+} from Eu^{2+}. Consequently, accessory mineral Eu/Eu* might not always be exclusively controlled by feldspar. The purpose of this paper is to highlight the potential complexity of Eu partitioning, by modeling changes in accessory mineral Eu/Eu* for three simple, plausible scenarios (changes in fO_2, feldspar fractionation, and open-system melting), as a basis for further discussion about interpreting accessory mineral Eu/Eu* in natural samples.

2. Methods

2.1. Construction of Partitioning Models

The concentrations of Sm, Eu, and Gd in accessory minerals, major minerals, and melt were calculated for average suprasolidus metapelite and metagreywacke (Figure 2) as functions of pressure and temperature using mineral modes and partition coefficients. Mineral modes were calculated by phase equilibrium modeling as described by Yakymchuk et al. (2017). Whole-rock mass fractions of Sm, Eu, and Gd were taken to be 5.9, 1.2, and 5.2 μg/g, respectively, reflecting the average values of shales (e.g., Condie, 1993). This corresponds to $Eu/Eu^*_{rock} = 0.66$.

There is considerable variability in the availability and quality of partitioning data. In recognition of this uncertainty, models were constructed with two sets of partition coefficients, referred to as "B94"—empirical partition coefficients from Bea et al. (1994)—and "modified composite" (MC)—a data set of partition coefficients compiled from multiple studies, modified slightly to reduce several discrepancies observed among calculations and observations in the first iterations of the model calculations (zircon and garnet: Rubatto & Hermann, 2007; Taylor et al., 2015; monazite: Stepanov et al., 2012; apatite: Watson & Green, 1981; plagioclase: Sun et al., 2017; alkali feldspar: Ren, 2004). The partitioning data used in each of these models are

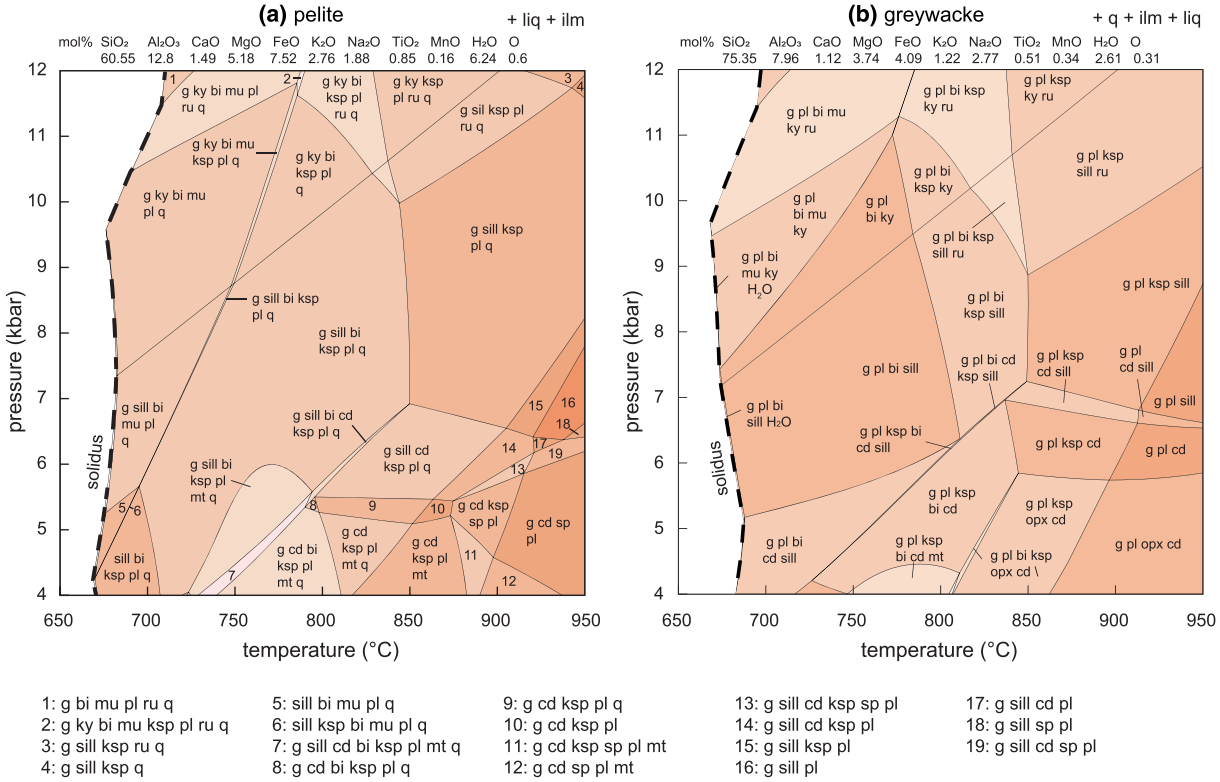

Figure 2. Phase equilibria of (a) average pelite and (b) greywacke used for the partitioning models of this study (Yakymchuk et al., 2017).

described in more detail in Texts S1 and S2 of the supporting information and summarized in Table 1. All partition coefficients (K_d^x, x = element or ion of interest) are mineral:melt unless specifically stated.

The advantages of the B94 models are as follows: (1) The estimated peak metamorphic temperature of the rocks from which the partitioning data were estimated (750°C) is lower than the experimental/magmatic temperatures of most trace element partitioning studies, and (2) the rocks from which the data were estimated are similar to the modeled compositions of this study (i.e., peraluminous migmatites). The B94 models do not account for the temperature or pressure dependence of partitioning or the presence of Eu^{2+} in accessory minerals, and the samples from which these data were estimated are more reduced than many metasedimentary rocks (e.g., Ague, 1991; Diener & Powell, 2010; Spear, 1993). The advantages of the MC models are that they account for the temperature dependence of partitioning and include both Eu^{2+} and Eu^{3+} in each accessory mineral.

2.2. Calculating Whole-Rock Eu Valence for Partitioning Models

The Eu species Eu^{3+} and Eu^{2+} were treated independently. Values of K_d^{Eu3+} were taken as the geometric mean of K_d^{Sm} and K_d^{Gd}, whereas it was assumed that $K_d^{Eu2+} = K_d^{Sr}$ (Philpotts, 1970) due to the near-identical size and ionic radius of Eu^{2+} and Sr^{2+} (Shannon, 1976). We assumed that the bulk-rock Eu^{2+}/Eu^{3+} ratios are reasonably approximated by the equations of Burnham et al. (2015), who measured Eu valence in experimental silicate melts as functions of temperature, fO_2 and melt composition. Burnham et al. (2015) found that contours of constant Eu^{2+}/Eu^{3+} were parallel to the fayalite-magnetite-quartz buffer in plots of fO_2 versus T, demonstrating that Eu valence was controlled by Fe^{2+}-Fe^{3+} redox. This suggests that the *relative* changes in Eu valence should be reasonably approximated by fO_2 for systems in which fO_2 is controlled by Fe^{2+}-Fe^{3+} mineral equilibrium (among magnetite-spinel, ilmenite, biotite, and garnet in our models). However, the *absolute values* of bulk rock and mineral Eu^{2+}/Eu^{3+} might be different in real (semi-)pelitic systems which differ from the experiments of Burnham et al. (2015) in that they are outside of their investigated compositional range (mostly mafic-intermediate), at lower temperature, and they contain minerals (the experiments of Burnham et al., 2015, were strictly on melts)

Table 1
Mineral:Melt K_d Used for Sm, Eu, and Gd Partitioning Modeling

Model		Monazite	Zircon	Garnet	Apatite	Plagioclase	Alkali feldspar	Biotite	Muscovite	Cordierite
B94	Sm^{3+}	75,289	3.79	0.45	1,105	1.45	0.42	0.06	0.06	0.10
	Eu^{2+}	—	—	0.01	—	1.25	0.77	0.01	0.01	0.12
	Eu^{3+}	84,934	5.91	1.49	1,535	1.72	0.50	0.08	0.08	0.17
	Gd^{3+}	95,815	9.21	4.95	2,133	2.05	0.60	0.10	0.10	0.29
Modified-Composite	Sm^{3+}	$50 \cdot 10^{\left(\frac{4,373.9}{T} - 1.0034\right)}$	$10^{\left(\frac{4,765.0}{T} - 3.3096\right)}$	$10^{\left(\frac{5,424.0}{T} - 4.1211\right)}$	$10^{\left(\frac{4,037.9}{T} - 1.7169\right)}$	$0.1 \cdot K_d^{Eu2+}$	$0.1 \cdot K_d^{Eu2+}$	—	—	—
	Eu^{2+}	$10^{\left(\frac{4,317.3}{T} - 3.8397\right)}$	$10^{\left(\frac{4,838.2}{T} - 5.4992\right)}$	$10^{\left(\frac{4,266.1}{T} - 5.0498\right)}$	$10^{\left(\frac{-738.33}{T} + 0.9258\right)}$	Sun et al. (2017)	Ren (2004), Sr equation	—	—	—
	Eu^{3+}	$50 \cdot 10^{\left(\frac{4,317.3}{T} - 1.0125\right)}$	$10^{\left(\frac{4,838.2}{T} - 3.1581\right)}$	$10^{\left(\frac{4,266.1}{T} - 2.8259\right)}$	$10^{\left(\frac{4,359.3}{T} - 1.9877\right)}$	$0.1 \cdot K_d^{Eu2+}$	$0.1 \cdot K_d^{Eu2+}$	—	—	—
	Gd^{3+}	$50 \cdot 10^{\left(\frac{4,254.2}{T} - 1.0158\right)}$	$10^{\left(\frac{5,147.7}{T} - 3.2562\right)}$	$10^{\left(\frac{3,470.9}{T} - 1.8673\right)}$	$10^{\left(\frac{4,670.0}{T} - 2.2498\right)}$	$0.1 \cdot K_d^{Eu2+}$	$0.1 \cdot K_d^{Eu2+}$	—	—	—

which might impart their own crystal-chemistry influence on Eu^{2+}/Eu^{3+} in their structures (e.g., Philpotts, 1970). Therefore, the models should only be interpreted semiquantitatively, in terms of order-of-magnitude change and trends.

Models were calculated with fixed O concentrations, corresponding to slightly oxidized bulk compositions ($Fe^{3+}/Fe^{total} = 0.15$; Yakymchuk et al., 2017) that produce ilmenite ± magnetite (e.g., Diener & Powell, 2010), consistent with observations from many natural metapelites. Calculated $\log_{10}fO_2$ in the models varies between ~FMQ_{+1} and FMQ_{+3}, where FMQ is the fayalite-magnetite-quartz buffer and the subscript indicates logarithmic deviations from the buffer. Such values are relatively common in metasedimentary granulites (e.g., Boger et al., 2012; Yakymchuk et al., 2019) and typical of many lower-crustal rocks in general (Bucholz & Kelemen, 2019). No explicit fO_2 buffer was imposed on the calculations, as that would require that O concentrations vary as a function of T, P, and the compositions of Fe^{2+}-Fe^{3+} solid solutions to maintain the buffer (i.e., not a closed system). Values of Eu^{3+}/Eu^{total} vary approximately linearly over this fO_2 range (Burnham et al., 2015). For significantly more reduced (<FMQ_{-4}) or oxidized rocks (>FMQ_{+8}), the equations of Burnham et al. (2015) predict Eu to be monovalent: Eu^{2+} or Eu^{3+}, respectively. Our calculations are not applicable to natural systems at these fO_2 extremes (such as graphite-pyrite-bearing metapelites; Connolly & Cesare, 1993).

2.3. Model Scenarios

(1) In the equilibrium closed-system partitioning models, partition coefficients were used to calculate concentrations of Sm, Eu, and Gd in each relevant mineral as functions of mineral modes, temperature, and Eu^{2+}/Eu^{3+} ratio. (2) The models of Eu fractionation by feldspar crystallization were calculated along an isobaric cooling path at 6 kbar. The models began at 950°C with rare earth element (REE) equilibrium among all phases. The REE incorporated into plagioclase and alkali feldspar as they grew was incrementally removed from the effective whole-rock composition at 1° K cooling intervals. All other aspects of these models were assumed to be in equilibrium (e.g., mineral modes, major-element compositions, and REE partitioning among all other phases) to specifically isolate the influence of feldspar fractionation on accessory mineral Eu anomalies. For portions of the modeled cooling path in which the mode of either plagioclase or alkali feldspar decreased, a proportionate amount of the previously fractionated REE was added back into the effective bulk-composition. (3) For the models of melt extraction during isobaric heating, REE equilibrium was maintained among all phases. When the melt fraction reached 7 mol%, approximately the melt connectivity threshold (Rosenberg & Handy, 2005), the major-element equivalent of 6 mol% melt was removed from the model composition (leaving 1% remaining) along with proportionate amounts of Sm, Eu, and Gd. Although the exact value of this melt connectivity threshold will depend on grainsize, grain shape, and deformation, this approach is used for consistency with the now common melt-reintegration method used by Korhonen et al. (2013) to estimate the protolith composition of residual granulites (this approach is the inverse of theirs). The weight fractions of accessory minerals were also modified by each melt extraction step in accordance with their solubilities (e.g., Yakymchuk, 2017).

3. Results

Results of the models are tabulated in Data Sets S1–S16, which are available through the EarthChem community data repository (Holder et al., 2020).

3.1. Models of Equilibrium, Unbuffered, Closed-System Metamorphism

Contours of oxygen fugacity ($\log_{10}fO_2$), oxygen fugacity relative to the fayalite-magnetite-quartz buffer ($\log_{10}fO_{2\ rock}$-$\log_{10}fO_{2\ FMQ}$), and Eu valence (Eu^{3+}/Eu^{total}) as functions of pressure and temperature are shown in Figure 3. Contours of $\log_{10}fO_{2\ rock}$-$\log_{10}fO_{2\ FMQ}$ (Figures 3c and 3d) parallel reactions among the Fe^{2+}-Fe^{3+} minerals (ilmenite, magnetite-spinel, garnet, and biotite). At higher pressure, the contours closely parallel the rutile-in

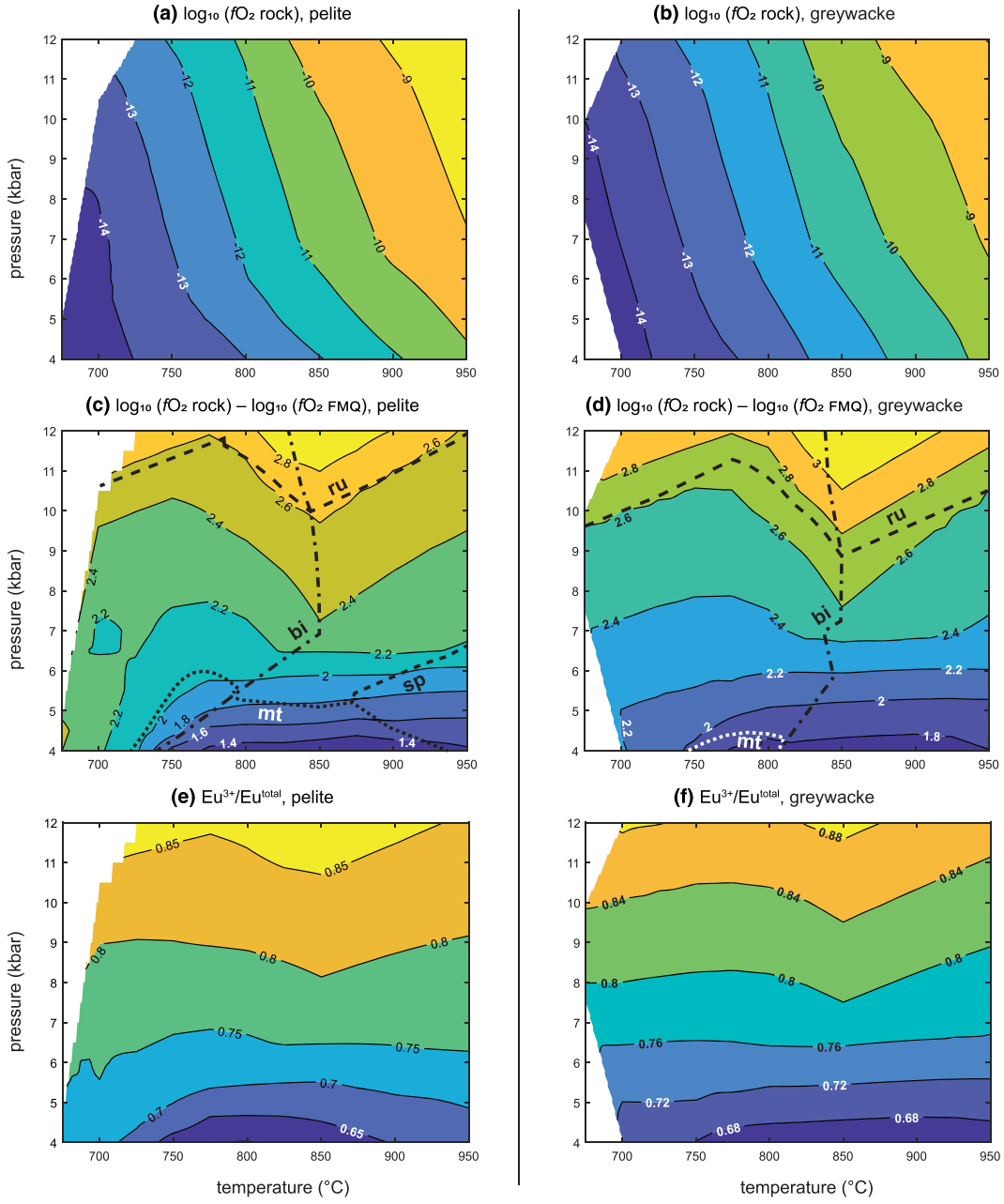

Figure 3. (a, b) The $\log_{10}fO_2$ of the modeled compositions. (c, d) Differences between $\log_{10}fO_2$ of the modeled compositions and the fayalite-magnetite-quartz buffer (FMQ). The shape of the contours is influenced by reactions among the Fe^{2+}–Fe^{3+} minerals—ilmenite, magnetite, garnet, and biotite—most notably the rutile-in reaction with increasing pressure (involving ilmenite breakdown and garnet growth), the magnetite-spinel-in reactions with decreasing pressure, and the biotite-out reaction with increasing temperature. (e, f) The ratio Eu^{3+}/Eu^{total} used to calculate Eu partitioning, which was calculated from fO_2, T, and melt composition (Burnham et al., 2015).

reaction, which involves breakdown of ilmenite to form garnet and rutile with increasing pressure; the slope of this reaction changes between 750°C and 850°C due to the breakdown of biotite. At lower pressure, the contours become more closely spaced, following magnetite-spinel stability, with a notable "trough" at ~750°C.

Contours of Eu^{3+}/Eu^{total} (Figures 3e and 3f) are similar to the contours of $\log_{10}fO_{2\ rock} - \log_{10}fO_{2\ FMQ}$ (Figures 3c and 3d), as expected from the Fe redox-controlled Eu-redox equations used in the models

(Burnham et al., 2015). The overall changes in Eu^{3+}/Eu^{total} across the models (675–950°C, 4–12 kbar) is 0.2–0.3 in both pelite and greywacke. The values of Eu^{3+}/Eu^{total} are primarily functions of pressure, due to the pressure-dependence of oxide stability, with slight deflection associated with biotite breakdown, as mentioned in the previous paragraph.

Calculated Eu/Eu* in the accessory minerals and garnet in the MC models are shown in Figure 4. The values for each mineral are ~0.6–0.7 at higher pressure and 0.4–0.5 at lower pressure. At lower temperature, where all three accessory minerals are abundant, the contours of Eu/Eu* essentially parallel the contours of whole-rock Eu^{3+}/Eu^{total} (Figures 3e and 3f). However, at ~850°C (pelite) and ~900°C (greywacke), contours of Eu/Eu* are more temperature dependent; this change occurs as the mode of monazite decreases exponentially, until it is not stable. For the B94 models, accessory mineral Eu/Eu* parallels whole-rock Eu^{3+}/Eu^{total} (Figure S1), because accessory mineral $K_d^{Eu2+} = 0$. Calculated Eu/Eu* anomalies of plagioclase and melt in the MC model are shown in Figure 5. Values of Eu/Eu* in feldspars and melt decrease with increasing temperature and show little pressure dependence, except for the B94 greywacke model (Figure S2) in which plagioclase and melt Eu/Eu* show a stronger pressure dependence near the solidus.

Figure 6 shows the proportion of each phase, their total Eu content, and their Eu/Eu* from the MC models along a hypothetical clockwise *P-T* path consisting of isobaric heating at 10 kbar to 850°C, isothermal decompression at 850°C to 5 kbar, and isobaric cooling at 5 kbar to 675°C. As described above, feldspars and melt Eu/Eu* changes most significantly with temperature, whereas Eu/Eu* of the accessory minerals and garnet ($K_d^{Eu3+} \gg K_d^{Eu2+}$) change most significantly with pressure. The total change in accessory mineral Eu/Eu* along such a *P-T* path is similar in all models: ~ −0.1 to −0.2. Pressure-temperature paths that pass through lower-pressure and higher-temperature conditions, where magnetite-spinel is stable, would result in slightly larger changes in Eu/Eu* for the accessory minerals and garnet (Figures 3e and 3f; e.g., Holder et al., 2018).

Figure 7 shows apatite Eu/Eu* as functions of *T*, *P*, feldspar wt%, and bulk-rock Eu^{3+}/Eu^{total} in the closed-system, equilibrium MC pelite model. Apatite is plotted, because it exhibits the largest *P-T* stability range of the accessory minerals; however, monazite and zircon exhibit similar relationships (Figures 4 and 6). Viewed together, these plots illustrate that the relationship of accessory mineral Eu/Eu* with feldspar is nonsystematic. In contrast, changes in pressure and temperature show strong consistent effects, due to changes in bulk-rock Eu valence (changes in fO_2, relative to the FMQ buffer) and monazite stability, respectively. Total changes in accessory mineral Eu/Eu* over the modeled *P-T* conditions are 0.2–0.3.

3.2. Models of Feldspar Fractionation

Figure 8 shows the results of the models in which REE are fractionated by feldspars during isobaric cooling and melt crystallization. Models were stopped when the weight fractions of the feldspars became essentially constant, making the fractionation calculations nonapplicable. For the pelite model, this occurred at 700°C, slightly above the calculated solidus. For linguistic simplicity, we refer to 700°C as "the solidus" for the pelite models in the following paragraphs. For the greywacke model, the weight fractions of feldspar are essentially constant at $T < 798$°C.

In all feldspar-fractionation models, the effective whole-rock Eu/Eu* decreases as the amount of feldspar increases. In the MC pelite model, the significant resorption of alkali feldspar as biotite begins to crystallize (at 813°C) results in a sharp increase in effective whole-rock Eu/Eu*, before continued plagioclase crystallization draws the value back down. The B94 pelite model does not show the same influence of the biotite-in reaction, due to much lower values of K_d^{Eu2+} in the alkali feldspar. Values of Eu/Eu* in accessory minerals and garnet are generally subparallel to the whole-rock values, with deviations due to changes in mineral modes and differences in K_d^{Eu3+} and K_d^{Eu2+} among minerals.

3.3. Models of Melt Extraction

Figure 9 shows the results of models in which REE were removed by step-wise melt extraction during isobaric heating based on their equilibrium values in melt. The results of the calculations differ substantially between the MC and B94 models.

For the MC models, melt extraction changes the bulk-rock Eu/Eu* very little from the initial value of 0.66. Accessory mineral and garnet Eu/Eu* show a total variability of 0.10–0.15 (pelite) and ~0.02 (greywacke).

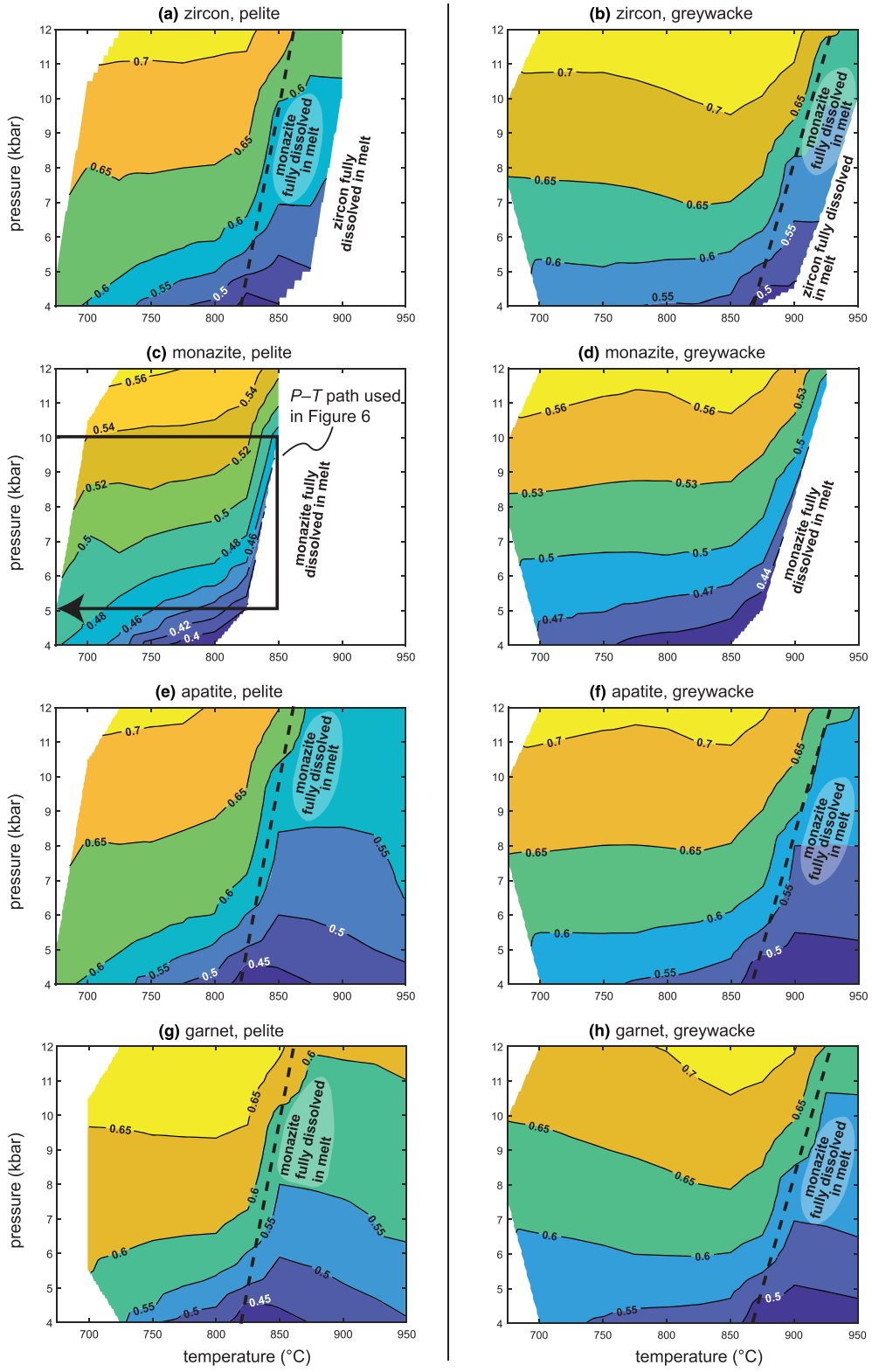

Figure 4. Calculated equilibrium Eu/Eu* anomalies of accessory minerals and garnet in the MC models: (a, b) zircon, (c, d) monazite, (e, f) apatite, and (g, h) garnet. Accessory mineral and garnet Eu/Eu* are primarily pressure dependent near the solidus, where the accessory minerals are abundant and the relative availability of Eu^{3+} and Eu^{2+} is controlled by fO_2. With increasing temperature, the fraction of each accessory minerals decreases exponentially, particularly monazite, thereby strongly influencing the distribution of REE, resulting in a stronger temperature dependence on Eu/Eu*.

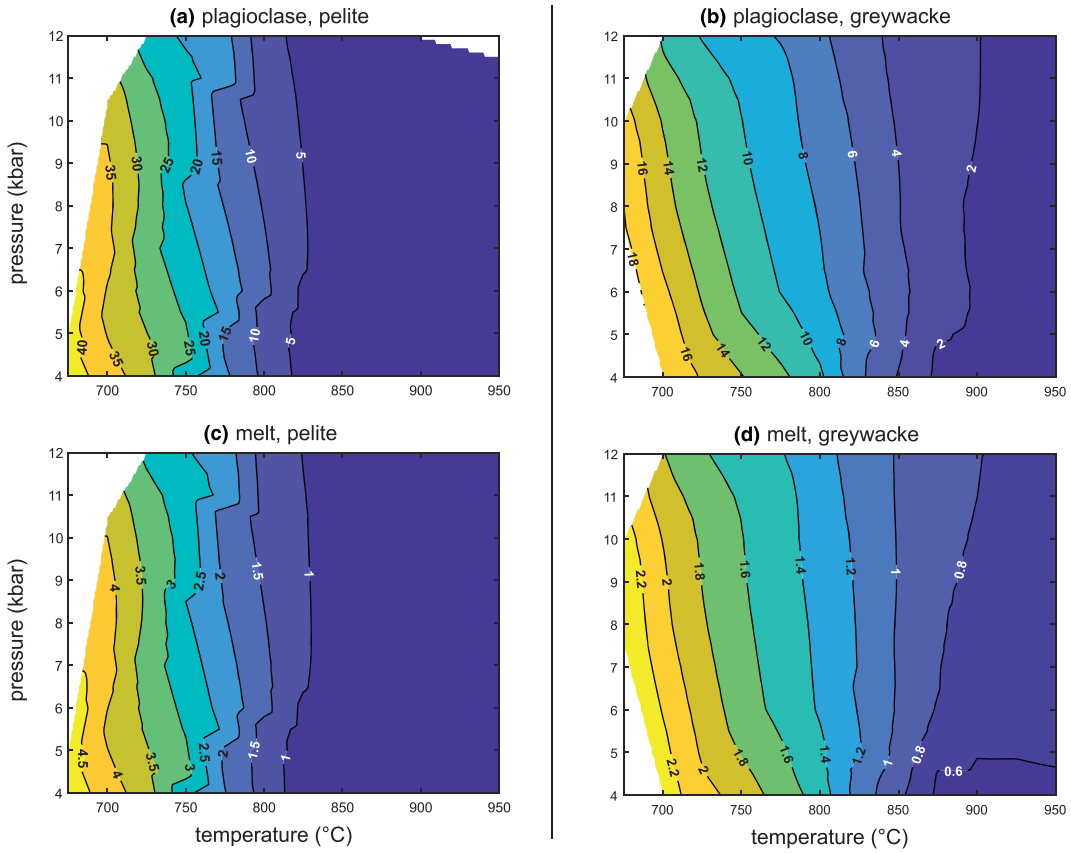

Figure 5. Calculated equilibrium Eu/Eu* of plagioclase and melt in the MC models: (a, b) plagioclase and (c, d) melt. In contrast to accessory mineral and garnet Eu/Eu* (Figure 4), feldspar and melt Eu/Eu* are strongly temperature dependent.

The greywacke models show less variability in Eu/Eu*, because less melt is produced and extracted. For the B94 models, melt extraction changes the bulk-rock Eu/Eu* more appreciably than in the MC models. Bulk-rock Eu/Eu* decreases from 0.66 to 0.53 (pelite) or 0.63 (greywacke). Values of accessory mineral and garnet Eu/Eu* generally follow the effective whole-rock Eu/Eu*, decreasing as melt is extracted.

The differences between results of the MC and B94 melt extraction models are primarily due to differences in the calculated Eu/Eu* of the melt. In the B94 models, the Eu/Eu* of the melt is 14 (greywacke) or 18 (pelite) at the solidus and remains greater than unity for most of the models, allowing for substantial removal of Eu relative to other REE during melt extraction. In the MC models, the Eu/Eu* of the melt is 2.4 (greywacke) or 4.5 (pelite) at the solidus and decreases below unity at 876°C (greywacke) or 830°C (pelite); although melt was extracted multiple times within this temperature range, the drawdown in whole-rock Eu/Eu* is negligible due to the relatively low Eu/Eu* and low total concentrations of REE in the melt.

4. Discussion

4.1. Controls on Equilibrium Mineral Eu/Eu*

Interpreting Eu/Eu* in minerals is complicated by the presence of both Eu^{2+} and Eu^{3+} in most metamorphic and igneous environments. The equilibrium Sm-Eu-Gd partitioning calculations shown in Figures 3–7 provide a starting point to understand the processes that control mineral Eu/Eu*.

Both feldspars and melt preferentially incorporate Eu^{2+} over Eu^{3+}, resulting in Eu/Eu* consistently greater than the whole-rock value. However, in all models, the values of feldspar and melt Eu/Eu* decrease by approximately an order of magnitude from 700°C to 950°C (Figure 5). This is due to several effects: (1) temperature- and composition-dependence of feldspar K_d's (e.g., plagioclase K_d^{Eu2+} decreases from 8.4 to

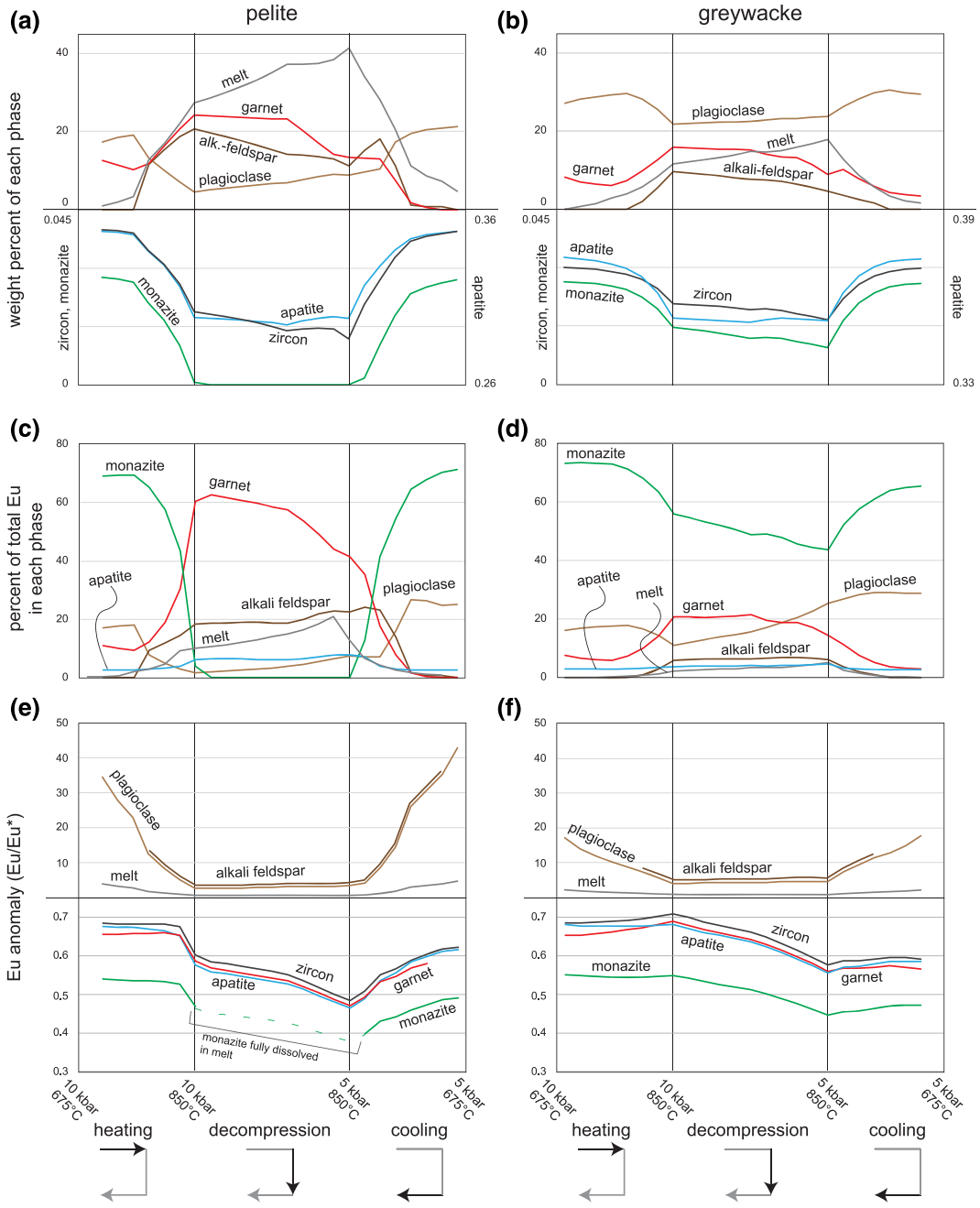

Figure 6. Values of Eu/Eu* in each phase are controlled by the temperature-dependent solubilities of accessory minerals and the pressure-dependent Eu^{3+}/Eu^{total} (Figures 3e and 3f). MC model results along the hypothetical *P-T* path shown in Figure 4c. Weight percent of phases along the path in (a) pelite and (b) greywacke. Percent of the total Eu in the system hosted by each phase in (c) pelite and (d) greywacke. Values of Eu/Eu* in each phase in (e) pelite and (f) greywacke.

0.33 between 700°C to 950°C at 10 kbar in the MC pelite model); (2) increase in the proportion of melt (Eu^{2+} must be shared among feldspars and melt); and (3) dissolution of accessory minerals, most prominently monazite (Figures 6 and 7), which requires that their Sm, Gd, and Eu (mostly Eu^{3+}) must be redistributed among the other phases.

The accessory minerals and garnet have very large Eu^{3+}/Eu^{2+} ratios (>10–100). Values of Eu/Eu* in these minerals is primarily controlled by the availability of Eu^{3+}. Contours of accessory mineral Eu/Eu*

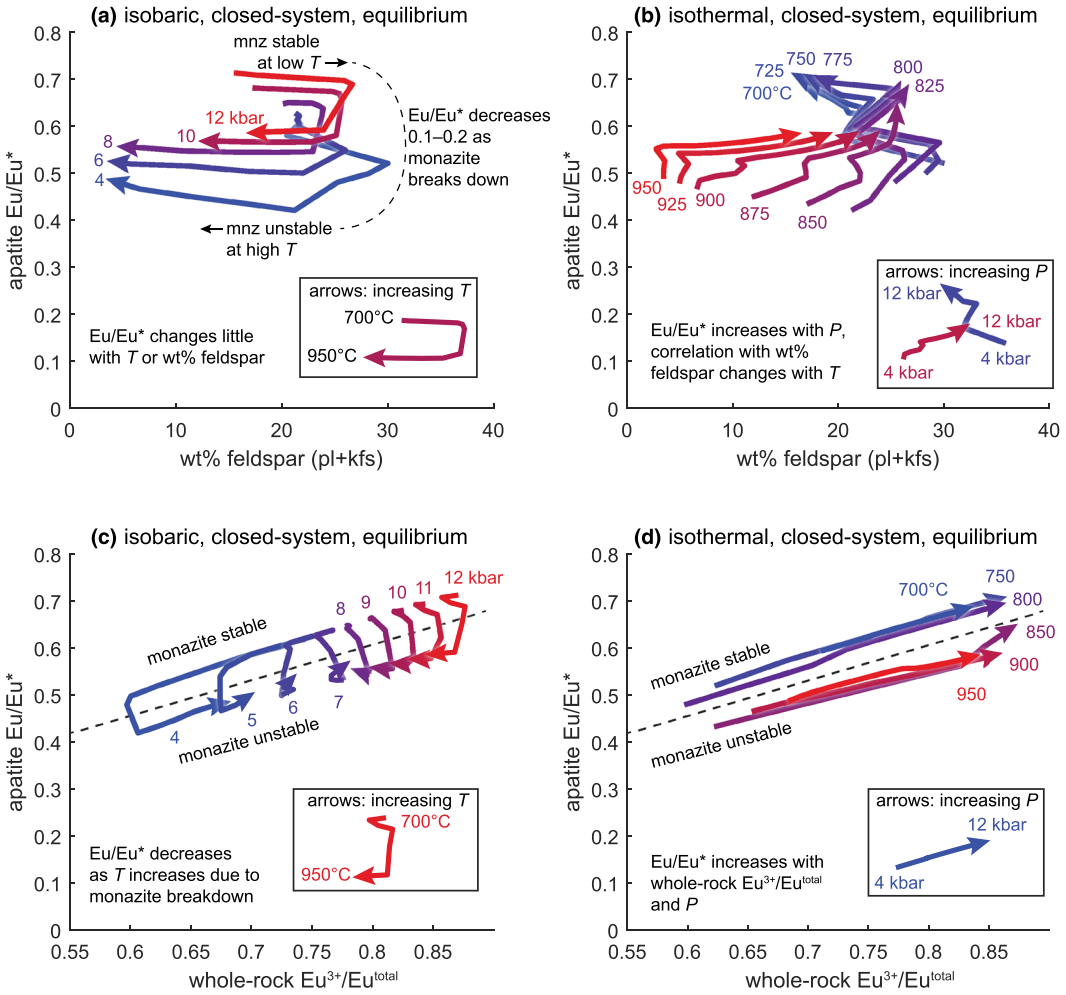

Figure 7. For the closed-system, equilibrium MC models, accessory mineral Eu anomalies exhibit strong positive correlations Eu^{3+}/Eu^{total}, which is primarily a function of pressure (Figure 4) and with monazite stability. In contrast, correlations with the wt% feldspar are inconsistent and variable, illustrating that, at equilibrium, wt% feldspar has minimal influence on accessory mineral Eu/Eu*. (a) Apatite Eu/Eu* as functions of wt% feldspar and temperature at constant pressure. (b) Apatite Eu/Eu* as functions of wt% feldspar and pressure at constant temperature. (c) Apatite Eu/Eu* as functions of whole-rock Eu^{3+}/Eu^{total} and temperature at constant pressure. (d) Apatite Eu/Eu* as functions of whole-rock Eu^{3+}/Eu^{total} and pressure at constant temperature. In all panels, apatite Eu/Eu* from the MC pelite model is shown. Apatite is plotted because it is stable at all modeled *P-T* conditions; monazite and zircon show similar Eu/Eu* patterns for the *P-T* conditions at which they are stable (Figure 4).

(Figure 4) are subparallel to the whole-rock Eu^{3+}/Eu^{total} contours (Figures 3e and 3f), which is governed by fO_2 (in the B94 models, this is the only control). An exception to this is, at ~850°C (pelite) and ~900°C (greywacke), the amount of monazite decreases exponentially until it becomes fully dissolved in the melt (Figure 4), causing the accessory mineral Eu/Eu* contours to deviate from the whole-rock Eu^{3+}/Eu^{total} contours.

Most importantly for this study, in the equilibrium closed-system models, there is no systematic correlation between feldspar abundance and accessory mineral Eu/Eu*. Apparent correlations occur for some *P-T* conditions, but these vary in sign and magnitude (Figure 7a and 7b) and are more appropriately attributed to changes in pressure and temperature, which influence modeled Eu^{3+}/Eu^{total} and the mode of monazite, respectively (Figure 7c and 7d). This lack of a clear relationship with the amount of feldspar is expected, because feldspars and accessory minerals are predominantely competing for different species of Eu (Eu^{2+} and Eu^{3+}, respectively; e.g., Kohn & Kelly, 2017). Maximum changes in

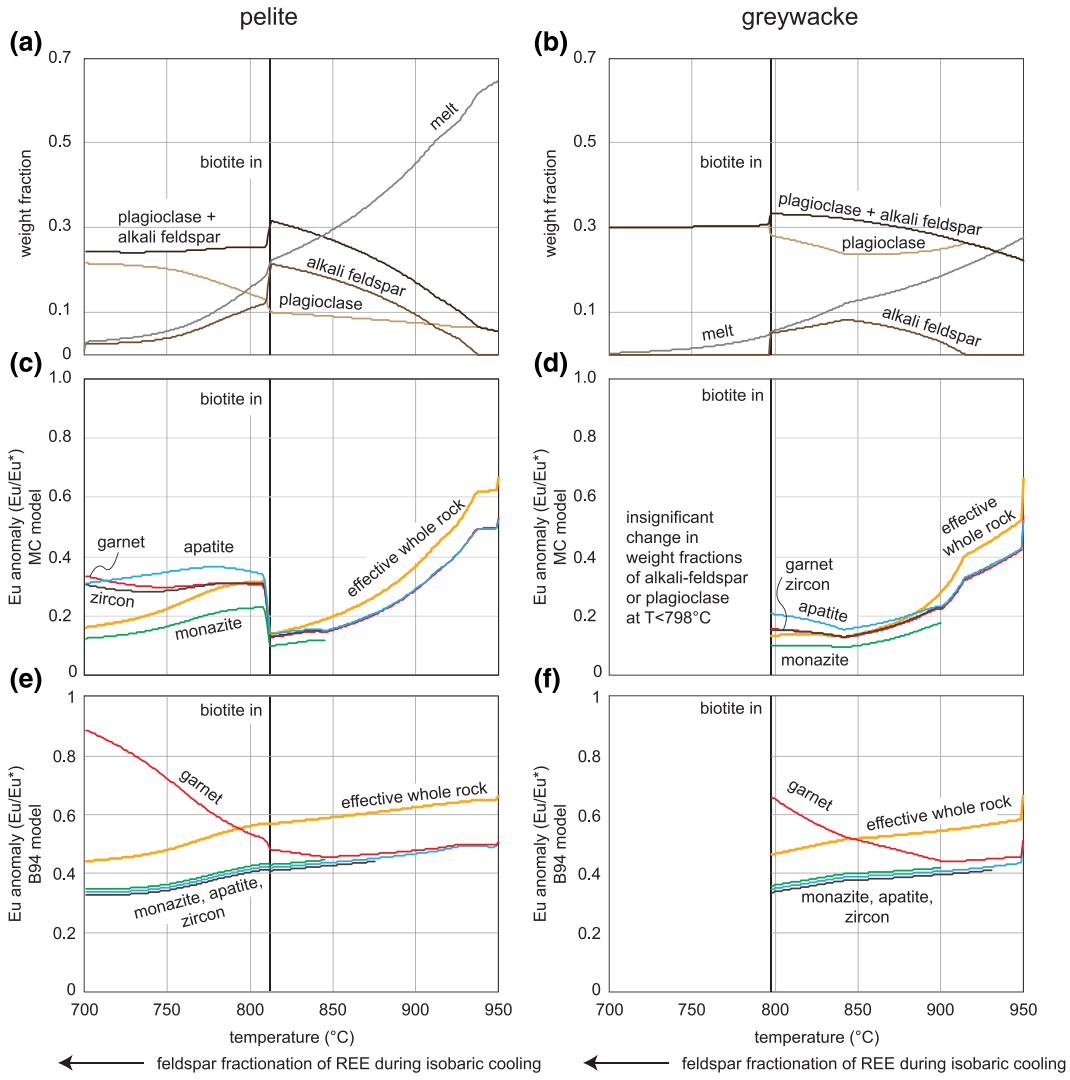

Figure 8. The fractionation of Eu by feldspar growth can decrease Eu/Eu* in accessory minerals and garnet. (a) Weight fractions of plagioclase, alkali feldspar, and melt in the model pelite. (b) Weight fractions of plagioclase, alkali feldspar, and melt in the model greywacke. (c) Effective whole-rock, garnet, and accessory mineral Eu/Eu* for the MC pelite model. The large increase in Eu/Eu* at ~810°C is due to alkali feldspar resorption during biotite growth. (d) Effective whole-rock, garnet, and accessory mineral Eu/Eu* for the MC greywacke model. Model was ended at 798°C, because the changes in the weight fractions of feldspars are minimal at lower temperature. (e) Effective whole-rock, garnet, and accessory mineral Eu/Eu* for the B94 pelite model. The smaller changes in Eu/Eu* relative to the MC model are due to lower feldspar K_d^{Eu2+}, particularly for the alkali feldspar. (f) Effective whole-rock, garnet, and accessory mineral Eu/Eu* for the B94 greywacke model.

equilibrium accessory mineral Eu/Eu* are predicted to be ~0.2–0.3 for the modeled suprasolidus conditions. Due to the strong pressure dependence of accessory mineral Eu/Eu* in the models, clockwise *P-T* paths are predicted to result in a net decrease in Eu/Eu*, whereas counterclockwise paths are predicted to result in a net increase in Eu/Eu*.

4.2. Open System Effects on Mineral Eu/Eu*

4.2.1. Fractionation of Eu by Feldspar Crystallization

The calculations shown in Figure 8 support the hypothesis that feldspar growth and breakdown can significantly influence accessory mineral Eu/Eu* if the REE incorporated into feldspar are effectively fractionated from the rest of the rock. For the MC models, crystallization of 10% feldspar resulted in a decrease in

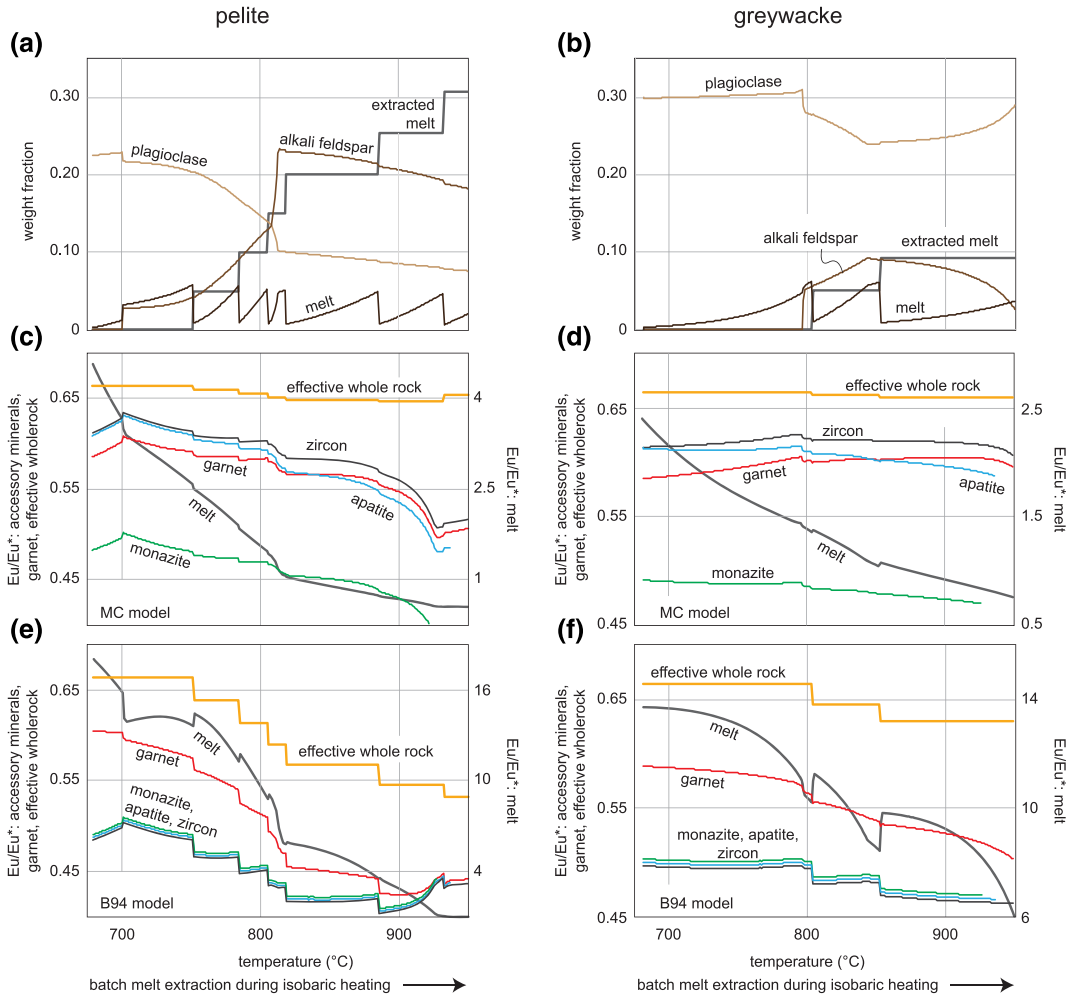

Figure 9. Melt extraction can decrease the effective whole-rock Eu/Eu* and thereby decrease Eu/Eu* of residual minerals; however, the modeled magnitude of this decrease is strongly dependent on the partitioning data used. (a) Weight fractions of plagioclase, alkali feldspar, melt (remaining in the system), and cumulative extracted melt in the pelite model and (b) in the greywacke model. Whole-rock and mineral Eu/Eu* in the (c) MC pelite model, (d) MC greywacke model, (e) B94 pelite model, and (f) B94 greywacke model. Relative to the MC models, the B94 models show larger drawdown in whole-rock Eu/Eu* by melt extraction, because the melt was calculated to have higher REE concentrations and larger Eu/Eu*.

accessory mineral Eu/Eu* of ~0.15, with a maximum possible decrease of ~0.4; for the B94 models, the corresponding decrease was smaller but not insignificant: ~0.05 for 10% feldspar crystallization, with a maximum possible decrease of ~0.15. However, application of these generalizations to real rocks is complicated by the recognition that alkali feldspar and plagioclase modes are unlikely to change monotonically during crystallization; they grow/breakdown as functions of their miscibility, and due to reactions with garnet (such as the "GASP" reaction), incongruent versus congruent melting, melt crystallization and reactions with micas. For example, the MC pelite model (Figure 8c) shows accessory mineral Eu/Eu* with increases and decreases of >0.1 during cooling as a result of feldspar crystallization at high temperature then feldspar resorption and mica crystallization at lower temperature. Another complication is that Eu^{2+} diffusivity in feldspar, if similar to Sr diffusivity, is ~4 orders of magnitude higher than REE^{3+} diffusivity (Cherniak, 2003; Cherniak & Watson, 1992, 1994); fractionation of Eu by feldspar growth might therefore be limited in very high-temperature systems. Nevertheless, the very large changes in accessory mineral Eu/Eu* observed in some samples (≥0.4, Figure 1; e.g., Rubatto et al., 2006), likely require some degree of Eu fractionation by feldspar growth.

4.2.2. Open-System Melting

In our models, melt Eu/Eu* was greater than whole-rock Eu/Eu* at all conditions. Therefore, extraction of melt from migmatites has the potential to decrease whole-rock Eu/Eu*, but the modeled magnitude of this decrease depends on the partitioning data used. Observations of leucosome:melanosome trace element ratios in natural samples from Bea et al. (1994) suggest that partial melt extraction can have a substantial influence on Eu/Eu* in residual minerals (Eu/Eu* changes >0.1 in the B94 models; Figure 8). However, the MC models suggest that open-system melting will have essentially no influence on accessory mineral Eu/Eu*. It is possible that the discrepancy in these results relates to how the partitioning data for the two models were estimated. The partitioning data of Bea et al. (1994) are based on mineral:leucosome trace element ratios; however, leucosomes rarely record initial melt compositions, due to fractional crystallization of feldspar (physical separation of feldspar from residual melt as the leucosome crystallizes: e.g., Brown et al., 2016; Sawyer, 1987). Consequently, the B94 models might have overpredicted the concentration of Eu^{2+} and Eu/Eu* in the melt.

5. Conclusions

As hypothesized by Rubatto et al. (2006), our models predict that growth of feldspar can significantly influence accessory mineral Eu/Eu*, but only if REE in feldspar are effectively fractionated from the rock. At equilibrium, the mode of feldspar has negligible/subordinate effects on accessory mineral Eu/Eu* compared to fO_2 and the stability of monazite (for the suprasolidus peraluminous rocks modeled). Feldspars do not strongly influence accessory mineral Eu/Eu* at equilibrium, because feldspars and accessory minerals predominantly incorporate different Eu species (Eu^{2+} and Eu^{3+}, respectively; e.g., Kohn & Kelly, 2017).

Whereas Y + heavy REE (HREE) partitioning among accessory minerals and garnet is relatively well understood (e.g. Pyle et al., 2001), Eu partitioning is highly complex. This makes interpretation of Eu/Eu* more difficult than Y + HREE, but might allow for a broader range of geological processes to be investigated with petrochronology, particularly open-system processes such as dehydration, fluid-rock interaction, partial melting, and magma crystallization. The models presented here provide a basis for further study but are limited in application to suprasolidus peraluminous rocks. The models are also limited in theory by available partitioning data and a lack of quantification on the crystal-chemical effects on Eu valence in minerals. To fully understand accessory mineral Eu/Eu*, the roles of other minerals (e.g., allanite, amphibole, titanite in metabasites, and intermediate rocks) also needs to be assessed. In addition, systematic assessments of Eu/Eu* in natural samples, as have been undertaken for mineral Y + HREE concentrations, are needed (e.g., Bea & Montero, 1999; Foster et al., 2000; Hermann & Rubatto, 2003; Pyle & Spear, 1999).

Data Availability Statement

Tabulated results of the models in this paper can be found in the EarthChem community data repository (DOI: 10.26022/IEDA/111590).

Acknowledgments

This work was supported by the Morton K Blaustein Department of Earth and Planetary Sciences, Johns Hopkins University. The authors declare no conflicts of interest. The authors thank Miguel Cisneros and Pierre Lanari for their helpful reviews, which improved the presentation and discussion of this work.

References

Ague, J. J. (1991). Evidence for major mass transfer and volume strain during regional metamorphism of pelites. *Geology*, *19*(8), 855–858. https://doi.org/10.1130/0091-7613(1991)019<0855:EFMMTA>2.3.CO;2

Bea, F., & Montero, P. (1999). Behavior of accessory phases and redistribution of Zr, REE, Y, Th, and U during metamorphism and partial melting of metapelites in the lower crust: An example from the Kinzigite formation of Ivrea-Verbano, NW Italy. *Geochimica et Cosmochimica Acta*, *63*(7-8), 1133–1153. https://doi.org/10.1016/S0016-7037

Bea, F., Pereira, M. D., & Stroh, A. (1994). Mineral/leucosome trace-element partitioning in a peraluminous migmatite (a laser ablation-ICP-MS study). *Chemical Geology*, *117*(1-4), 291–312. https://doi.org/10.1016/0009-2541(94)90133-3

Boger, S. D., White, R. W., & Schulte, B. (2012). The importance of iron speciation (Fe^{+2}/Fe^{+3}) in determining mineral assemblages: An example from the high-grade aluminous metapelites of southeastern Madagascar. *Journal of Metamorphic Geology*, *30*(9), 997–1018. https://doi.org/10.1111/jmg.12001

Brown, C. R., Yakymchuk, C., Brown, M., Fanning, C. M., Korhonen, F. J., Piccoli, P. M., & Siddoway, C. S. (2016). From source to sink: Petrogenesis of Cretaceous anatectic granites from the Fosdick migmatite-granite complex, West Antarctica. *Journal of Petrology*, *57*(7), 1241–1278. https://doi.org/10.1093/petrology/egw039

Bucholz, C. E., & Kelemen, P. B. (2019). Oxygen fugacity at the base of the Talkeetna arc, Alaska. *Contributions to Mineralogy and Petrology*, *174*(10), 1, 79–27. https://doi.org/10.1007/s00410-019-1609-z

Buick, I. S., Hermann, J., Williams, I. S., Gibson, R. L., & Rubatto, D. (2006). A SHRIMP U–Pb and LA-ICP-MS trace element study of the petrogenesis of garnet–cordierite–orthoamphibole gneisses from the central zone of the Limpopo Belt, South Africa. *Lithos*, *88*(1–4), 150–172. https://doi.org/10.1016/j.lithos.2005.09.001

Burnham, A. D., Berry, A. J., Halse, H. R., Schofield, P. F., Cibin, G., & Mosselmans, J. F. W. (2015). The oxidation state of europium in silicate melts as a function of oxygen fugacity, composition and temperature. *Chemical Geology*, *411*, 248–259. https://doi.org/10.1016/j.chemgeo.2015.07.002

Cherniak, D. J. (2003). REE diffusion in feldspar. *Chemical Geology*, *193*(1–2), 25–41. https://doi.org/10.1016/S0009-2541(02)00246-2

Cherniak, D. J., & Watson, E. B. (1992). A study of strontium diffusion in K-feldspar, Na-K feldspar and anorthite using Rutherford backscattering spectroscopy. *Earth and Planetary Science Letters*, *113*(3), 411–425. https://doi.org/10.1016/0012-821X(92)90142-I

Cherniak, D. J., & Watson, E. B. (1994). A study of strontium diffusion in plagioclase using Rutherford backscattering spectroscopy. *Geochimica et Cosmochimica Acta*, *58*(23), 5179–5190. https://doi.org/10.1016/0016-7037(94)90303-4

Cioffi, C. R., Campos Neto, M. C., Möller, A., & Rocha, B. C. (2019). Titanite petrochronology of the southern Brasília Orogen basement: Effects of retrograde net-transfer reactions on titanite trace element compositions. *Lithos*, *344-345*, 393–408. https://doi.org/10.1016/j.lithos.2019.06.035

Condie, K. C. (1993). Chemical composition and evolution of the upper continental crust: Contrasting results from surface samples and shales. *Chemical Geology*, *104*(1–4), 1–37. https://doi.org/10.1016/0009-2541(93)90140-E

Connolly, J. A. D., & Cesare, B. (1993). C-O-H-S fluid composition and oxygen fugacity in graphitic metapelites. *Journal of Metamorphic Geology*, *11*(3), 379–388. https://doi.org/10.1111/j.1525-1314.1993.tb00155.x

Diener, J. F. A., & Powell, R. (2010). Influence of ferric iron on the stability of mineral assemblages. *Journal of Metamorphic Geology*, *28*(6), 599–613. https://doi.org/10.1111/j.1525-1314.2010.00880.x

Engi, M. (2017). Petrochronology based on REE-minerals: Monazite, allanite, xenotime, apatite. *Reviews in Mineralogy and Geochemistry*, *83*(1), 365–418. https://doi.org/10.2138/rmg.2017.83.12

Engi, M., Lanari, P., & Kohn, M. J. (2017). Significant ages—An introduction to petrochronology. *Reviews in Mineralogy and Geochemistry*, *83*(1), 1–12. https://doi.org/10.2138/rmg.2017.83.1

Ferry, J. M., & Watson, E. B. (2007). New thermodynamic models and revised calibrations for the Ti-in-zircon and Zr-in-rutile thermometers. *Contributions to Mineralogy and Petrology*, *154*(4), 429–437. https://doi.org/10.1007/s00410-007-0201-0

Finger, F., & Krenn, E. (2007). Three metamorphic monazite generations in a high-pressure rock from the Bohemian Massif and the potentially important role of apatite in stimulating polyphase monazite growth along a PT loop. *Lithos*, *95*(1–2), 103–115. https://doi.org/10.1016/j.lithos.2006.06.003

Foster, G., Gibson, H. D., Parrish, R., Horstwood, M., Fraser, J., & Tindle, A. (2002). Textural, chemical and isotopic insights into the nature and behaviour of metamorphic monazite. *Chemical Geology*, *191*(1–3), 1–3–207. https://doi.org/10.1016/S0009-2541(02)00156-0, 183

Foster, G., Kinny, P., Vance, D., Prince, C., & Harris, N. (2000). The significance of monazite U–Th–Pb age data in metamorphic assemblages; a combined study of monazite and garnet chronometry. *Earth and Planetary Science Letters*, *181*(3), 327–340. https://doi.org/10.1016/S0012-821X(00)00212-0

Garber, J. M., Hacker, B. R., Kylander-Clark, A. R. C., Stearns, M. A., & Seward, G. (2017). Controls on trace element uptake in metamorphic titanite: Implications for petrochronology. *Journal of Petrology*, *58*(6), 1031–1057. https://doi.org/10.1093/petrology/egx046

Gratz, R., & Heinrich, W. (1997). Monazite-xenotime thermobarometry: Experimental calibration of the miscibility gap in the binary system CePO4-YPO4. *American Mineralogist*, *82*(7–8), 772–780. https://doi.org/10.2138/am-1997-7-816

Hacker, B., Kylander-Clark, A., & Holder, R. (2019). REE partitioning between monazite and garnet: Implications for petrochronology. *Journal of Metamorphic Geology*, *37*(2), 227–237. https://doi.org/10.1111/jmg.12458

Hayden, L. A., Watson, E. B., & Wark, D. A. (2008). A thermobarometer for sphene (titanite). *Contributions to Mineralogy and Petrology*, *155*(4), 529–540. https://doi.org/10.1007/s00410-007-0256-y

Hermann, J., & Rubatto, D. (2003). Relating zircon and monazite domains to garnet growth zones: Age and duration of granulite facies metamorphism in the Val Malenco lower crust. *Journal of Metamorphic Geology*, *21*(9), 833–852. https://doi.org/10.1046/j.1525-1314.2003.00484.x

Hokada, T., & Harley, S. L. (2004). Zircon growth in UHT leucosome: Constraints from zircon-garnet rare earth elements (REE) relations in Napier complex, East Antarctica. *Journal of Mineralogical and Petrological Sciences*, *99*(4), 180–190. https://doi.org/10.2465/jmps.99.180

Holder, R., Yakymchuk, C., Viete, D. (2020). Modeled mineral Eu anomalies in suprasolidus metasediments, version 1.0. Interdisciplinary Earth Data Alliance (IEDA). https://doi.org/10.26022/IEDA/111590

Holder, R. M., Hacker, B. R., Horton, F., & Rakotondrazafy, A. F. M. (2018). Ultrahigh-temperature osumilite gneisses in southern Madagascar record combined heat advection and high rates of radiogenic heat production in a long-lived high- T orogen. *Journal of Metamorphic Geology*, *36*(7), 855–880. https://doi.org/10.1111/jmg.12316

Holder, R. M., Hacker, B. R., Kylander-Clark, A. R. C., & Cottle, J. M. (2015). Monazite trace-element and isotopic signatures of (ultra)high-pressure metamorphism: Examples from the Western Gneiss region, Norway. *Chemical Geology*, *409*, 99–111. https://doi.org/10.1016/j.chemgeo.2015.04.021

Janots, E., Brunet, F., Goffé, B., Poinssot, C., Burchard, M., & Cemič, L. (2007). Thermochemistry of monazite-(La) and dissakisite-(La): Implications for monazite and allanite stability in metapelites. *Contributions to Mineralogy and Petrology*, *154*(1), 1–14. https://doi.org/10.1007/s00410-006-0176-2

Kelly, N. M., Clarke, G. L., & Harley, S. L. (2006). Monazite behaviour and age significance in poly-metamorphic high-grade terrains: A case study from the western Musgrave Block, central Australia11Abbreviations: After Kretz, 1983. *Lithos*, *88*(1-4), 100–134. https://doi.org/10.1016/j.lithos.2005.08.007

Kelly, N. M., & Harley, S. L. (2005). An integrated microtextural and chemical approach to zircon geochronology: Refining the Archaean history of the Napier complex, east Antarctica. *Contributions to Mineralogy and Petrology*, *149*(1), 57–84. https://doi.org/10.1007/s00410-004-0635-6

Kelsey, D. E., Clark, C., & Hand, M. (2008). Thermobarometric modelling of zircon and monazite growth in melt-bearing systems: Examples using model metapelitic and metapsammitic granulites. *Journal of Metamorphic Geology*, *26*(2), 199–212. https://doi.org/10.1111/j.1525-1314.2007.00757.x

Kohn, M. J. (2017). Titanite petrochronology. *Reviews in Mineralogy and Geochemistry*, *83*(1), 419–441. https://doi.org/10.2138/rmg.2017.83.13

Kohn, M. J., Corrie, S. L., & Markley, C. (2015). The fall and rise of metamorphic zircon. *American Mineralogist*, *100*(4), 897–908. https://doi.org/10.2138/am-2015-5064

Kohn, M. J., & Kelly, N. M. (2017). Petrology and geochronology of metamorphic zircon. *Microstructural Geochronology: Planetary Records Down to Atom Scale*, 35–61. https://doi.org/10.1002/9781119227250.ch2

Korhonen, F. J., Brown, M., Clark, C., & Bhattacharya, S. (2013). Osumilite-melt interactions in ultrahigh temperature granulites: Phase equilibria modelling and implications for the P-T-t evolution of the eastern ghats province, India. *Journal of Metamorphic Geology*, *31*(8), 881–907. https://doi.org/10.1111/jmg.12049

McDonough, W. F., & Sun, S.-s. (1995). The composition of the Earth. *Chemical Geology*, *120*(3-4), 223–253. https://doi.org/10.1016/0009-2541(94)00140-4

Mottram, C. M., Warren, C. J., Regis, D., Roberts, N. M. W., Harris, N. B. W., Argles, T. W., & Parrish, R. R. (2014). Developing an inverted Barrovian sequence; insights from monazite petrochronology. *Earth and Planetary Science Letters*, *403*, 418–431. https://doi.org/10.1016/j.epsl.2014.07.006

O'Brien, P. J., & Rötzler, J. (2003). High-pressure granulites: Formation, recovery of peak conditions and implications for tectonics. *Journal of Metamorphic Geology*, *21*(1), 3–20. https://doi.org/10.1046/j.1525-1314.2003.00420.x

Philpotts, J. A. (1970). Redox estimation from a calculation of Eu^{2+} and Eu^{3+} concentrations in natural phases. *Earth and Planetary Science Letters*, *9*(3), 257–268. https://doi.org/10.1016/0012-821X(70)90036-1

Pyle, J. M., & Spear, F. S. (1999). Yttrium zoning in garnet: Coupling of major and accessory phases during metamorphic reactions. *Geological Materials Research*, *1*(6), 1–49.

Pyle, J. M., Spear, F. S., Rudnick, R. L., & McDonough, W. F. (2001). Monazite–xenotime–garnet equilibrium in metapelites and a new monazite–garnet thermometer. *Journal of Petrology*, *42*(11), 2083–2107. https://doi.org/10.1093/petrology/42.11.2083

Ren, M. (2004). Partitioning of Sr, Ba, Rb, Y, and LREE between alkali feldspar and peraluminous silicic magma. *American Mineralogist*, *89*(8–9), 1290–1303. https://doi.org/10.2138/am-2004-8-918

Rosenberg, C. L., & Handy, M. R. (2005). Experimental deformation of partially melted granite revisited: Implications for the continental crust. *Journal of Metamorphic Geology*, *23*(1), 19–28. https://doi.org/10.1111/j.1525-1314.2005.00555.x

Rubatto, D. (2002). Zircon trace element geochemistry: Distribution coefficients and the link between U-Pb ages and metamorphism. *Chemical Geology*, *184*(1-2), 123–138. Retrieved from. www.elsevier.com/locate/chemgeo, https://doi.org/10.1016/S0009-2541(01)00355-2

Rubatto, D. (2017). Zircon: The metamorphic mineral. *Reviews in Mineralogy and Geochemistry*, *83*(1), 261–295. https://doi.org/10.2138/rmg.2017.83.10

Rubatto, D., Chakraborty, S., & Dasgupta, S. (2013). Timescales of crustal melting in the higher Himalayan crystallines (Sikkim, Eastern Himalaya) inferred from trace element-constrained monazite and zircon chronology. *Contributions to Mineralogy and Petrology*, *165*(2), 349–372. https://doi.org/10.1007/s00410-012-0812-y

Rubatto, D., & Hermann, J. (2007). Experimental zircon/melt and zircon/garnet trace element partitioning and implications for the geochronology of crustal rocks. *Chemical Geology*, *241*(1–2), 38–61. https://doi.org/10.1016/j.chemgeo.2007.01.027

Rubatto, D., Hermann, J., & Buick, I. S. (2006). Temperature and bulk composition control on the growth of monazite and zircon during low-pressure Anatexis (Mount Stafford, Central Australia). *Journal of Petrology*, *47*(10), 1973–1996. https://doi.org/10.1093/petrology/egl033

Sawyer, E. W. (1987). The role of partial melting and fractional crystallization in determining discordant migmatite leucosome compositions. *Journal of Petrology*, *28*(3), 445–473. https://doi.org/10.1093/petrology/28.3.445

Seydoux-Guillaume, A.-M., Wirth, R., Heinrich, W., & Montel, J.-M. (2002). Experimental determination of thorium partitioning between monazite and xenotime using analytical electron microscopy and X-ray diffraction Rietveld analysis. *European Journal of Mineralogy*, *14*(5), 869–878. https://doi.org/10.1127/0935-1221/2002/0014-0869

Shannon, R. D. (1976). Revised effective ionic radii and systematic studies of interatomie distances in halides and chalcogenides. *Acta Crystallographica*, *A32*, 751–767.

Shrestha, S., Larson, K. P., Duesterhoeft, E., Soret, M., & Cottle, J. M. (2019). Thermodynamic modelling of phosphate minerals and its implications for the development of P-T-t histories: A case study in garnet - monazite bearing metapelites. *Lithos*, *334-335*, 141–160. https://doi.org/10.1016/j.lithos.2019.03.021

Spear, F. S. (2010). Monazite–allanite phase relations in metapelites. *Chemical Geology*, *279*(1–2), 55–62. https://doi.org/10.1016/j.chemgeo.2010.10.004

Spear, F. S., & Pyle, J. M. (2010). Theoretical modeling of monazite growth in a low-Ca metapelite. *Chemical Geology*, *273*(1–2), 111–119. https://doi.org/10.1016/j.chemgeo.2010.02.016

Spear, F. S. (1993). *Metamorphic phase equilibria and pressure-temperature-time paths. Monograph/Mineralogical Society of America*. Washington, D.C.: Mineralogical Society of America.

Stepanov, A. S., Hermann, J., Rubatto, D., & Rapp, R. P. (2012). Experimental study of monazite/melt partitioning with implications for the REE, Th and U geochemistry of crustal rocks. *Chemical Geology*, *300-301*, 200–220. https://doi.org/10.1016/j.chemgeo.2012.01.007

Sun, C., Graff, M., & Liang, Y. (2017). Trace element partitioning between plagioclase and silicate melt: The importance of temperature and plagioclase composition, with implications for terrestrial and lunar magmatism. *Geochimica et Cosmochimica Acta*, *206*, 273–295. https://doi.org/10.1016/j.gca.2017.03.003

Taylor, R. J. M., Harley, S. L., Hinton, R. W., Elphick, S., Clark, C., & Kelly, N. M. (2015). Experimental determination of REE partition coefficients between zircon, garnet and melt: A key to understanding high-T crustal processes. *Journal of Metamorphic Geology*, *33*(3), 231–248. https://doi.org/10.1111/jmg.12118

Thomas, J. B., Watson, E. B., Spear, F. S., & Wark, D. A. (2015). TitaniQ recrystallized: Experimental confirmation of the original Ti-in-quartz calibrations. *Contributions to Mineralogy and Petrology*, *169*(3), 27. https://doi.org/10.1007/s00410-015-1120-0

Tomkins, H. S., Powell, R., & Ellis, D. J. (2007). The pressure dependence of the zirconium-in-rutile thermometer. *Journal of Metamorphic Geology*, *25*(6), 703–713. https://doi.org/10.1111/j.1525-1314.2007.00724.x

Wark, D. A., & Watson, E. B. (2006). TitaniQ: A titanium-in-quartz geothermometer. *Contributions to Mineralogy and Petrology*, *152*(6), 743–754. https://doi.org/10.1007/s00410-006-0132-1

Warren, C. J., Greenwood, L. V., Argles, T. W., Roberts, N. M. W., Parrish, R. R., & Harris, N. B. W. (2019). Garnet-monazite rare earth element relationships in sub-solidus Metapelites: A case study from Bhutan. *Geological Society Special Publication*, *478*(1), 145–166. https://doi.org/10.1144/SP478.1

Watson, E. B., & Green, T. H. (1981). Apatite/liquid partition coefficients for the rare earth elements and strontium. *Earth and Planetary Science Letters*, *56*(C), 405–421. https://doi.org/10.1016/0012-821X(81)90144-8

Yakymchuk, C. (2017). Behaviour of apatite during partial melting of metapelites and consequences for prograde suprasolidus monazite growth. *Lithos*, *274-275*, 412–426. https://doi.org/10.1016/j.lithos.2017.01.009

Yakymchuk, C., & Brown, M. (2014). Behaviour of zircon and monazite during crustal melting. *Journal of the Geological Society*, *171*(4), 465–479. https://doi.org/10.1144/jgs2013-115

Yakymchuk, C., Clark, C., & White, R. W. (2017). Phase relations, reactions sequences and petrochronology. *Reviews in Mineralogy and Geochemistry*, *83*(1), 13–53. https://doi.org/10.2138/rmg.2017.83.2

Yakymchuk, C., Rehm, A., Liao, Z., & Cottle, J. M. (2019). Petrochronology of oxidized granulites from southern Peru. *Journal of Metamorphic Geology*, *37*(6), 839–862. https://doi.org/10.1111/jmg.12501

Zack, T., & Kooijman, E. (2017). Petrology and geochronology of rutile. *Reviews in Mineralogy and Geochemistry*, *83*(1), 443–467. https://doi.org/10.2138/rmg.2017.83.14